

Estimate Sonic Mach Number in the Interstellar Medium with Convolutional Neural Network

TYLER SCHMALTZ,^{1,2} YUE HU*³,⁴ AND ALEX LAZARIAN⁴

¹*Department of Physics, University of Wisconsin-Madison, Madison, WI, 53706, USA*

²*Department of Astronomy, University of Wisconsin-Madison, Madison, WI, 53706, USA*

³*Institute for Advanced Study, 1 Einstein Drive, Princeton, NJ 08540, USA*

⁴*Department of Astronomy, University of Wisconsin-Madison, Madison, WI 53706, USA*

ABSTRACT

Understanding the role of turbulence in shaping the interstellar medium (ISM) is crucial for studying star formation, molecular cloud evolution, and cosmic ray propagation. Central to this is the measurement of the sonic Mach number (M_s), which quantifies the ratio of turbulent velocity to the sound speed. In this work, we introduce a convolutional neural network (CNN)-based approach for estimating M_s directly from spectroscopic observations. The approach leverages the physical correlation between increasing M_s and the shock-induced small-scale fluctuations that alter the morphological features in intensity, velocity centroid, and velocity channel maps. These maps, derived from 3D magnetohydrodynamic (MHD) turbulence simulations, serve as inputs for the CNN training. By learning the relationship between these structural features and the underlying turbulence properties, CNN can predict M_s under various conditions, including different magnetic fields and levels of observational noise. The median uncertainty of the CNN-predicted M_s ranges from 0.5 to 1.5 depending on the noise level. While intensity maps offer lower uncertainty, channel maps have the advantage of predicting the 3D M_s distribution, which is crucial in estimating 3D magnetic field strength. Our results demonstrate that machine-learning-based tools can effectively characterize complex turbulence properties in the ISM.

Keywords: Interstellar plasma (851) — Interstellar line emission (844) — Interstellar medium (803) — Magnetohydrodynamical simulations (1966) — Deep learning (1938)

1. INTRODUCTION

MHD turbulence plays a pivotal role as an influential factor shaping the evolution and structure of the interstellar medium (ISM; Larson 1981; Armstrong et al. 1995; Chepurnov & Lazarian 2010; Xu & Zhang 2017; Ha et al. 2022; Hu et al. 2022b). Namely, it contributes to many astrophysical processes in the ISM including but not limited to molecular cloud evolution (Ostriker et al. 2001; Federrath et al. 2008; Lazarian et al. 2012; Lazarian 2014; Hu et al. 2022; Vázquez-Semadeni et al. 2024), star formation (Mac Low & Klessen 2004; Crutcher 2004; McKee & Ostriker 2007; Federrath & Klessen 2012; Hu et al. 2021, 2022), cosmic ray propagation (Jokipii 1966; Ghilea et al. 2011; Xu & Yan 2013; Hu et al. 2022a; Xu 2022), Add Schlickeiser 2006 and

another 4 papers) characterization of the B-mode polarizations in the Cosmic Microwave Background (CMB; Pogosian 2014; Bracco et al. 2019). Despite MHD turbulence’s critical importance, our understanding of astrophysical implications remains incomplete.

Particularly for star formation, MHD turbulence can provide global support against the forces of gravity in molecular clouds (Elmegreen 1993; Wurster & Li 2018; Mignon-Risse, R. et al. 2023; Vázquez-Semadeni et al. 2024) but produce local density fluctuations serving as seeds of star formation (Mac Low & Klessen 2004; Krumholz & McKee 2005; McKee & Ostriker 2007; Burkhart 2018). The sonic Mach number, M_s , is a critical parameter in characterizing MHD turbulence, representing the ratio of the turbulent velocity to the sound speed. This ratio is indicative of fluid compressibility and is crucial for understanding star formation in molecular clouds. Over the years, a number of methods have been developed to measure M_s alongside other turbulent

parameters like the Alfvénic Mach number, M_A . One common approach involves analyzing the column density probability distribution functions (N-PDFs), which generally assume a lognormal distribution in regions dominated by turbulence (Vazquez-Semadeni 1994; Hill et al. 2008; Berkhuijsen & Fletcher 2008; Brunt, C. M. 2010; Ballesteros-Paredes et al. 2011; Federrath & Banerjee 2015; Burkhart 2018). The width or dispersion of the N-PDFs is closely related to M_s ; a larger M_s represents significant density fluctuations and consequently, a broader N-PDF. Several studies have explored the potential of estimating M_s from the skewness of the N-PDF (Kowal et al. 2007; Burkhart et al. 2009) and from the variance of column density (Padoan et al. 1997; Passot & Vázquez-Semadeni 1998; Burkhart & Lazarian 2012). Additionally, some studies have applied more complex functions, like the Tsallis function, to fit the N-PDFs. By analyzing the parameters of these fits, further estimations of M_s can be achieved (Esquivel & Lazarian 2010; Tofflemire et al. 2011). These statistical measures have provided crucial insights into the MHD turbulence’s properties within the cloud.

However, determining the spatial distribution of the M_s on the plane-of-the-sky (POS) still poses significant challenges, particularly due to the need for large data samples for the typical statistical methods. Estimating M_s in multi-phase ISM, such as neutral hydrogen (H I) and H α regions, adds further complexity. Additionally, variations in M_s along the line of sight (LOS) are critical for assessing the 3D distribution of magnetic field strength in these media (Lazarian et al. 2022; Hu & Lazarian 2023; Lazarian et al. 2024). In this work, we introduce a machine learning paradigm for estimating the M_s , since the morphological changes of density and intensity structures are associated with different M_s values. Highly supersonic media, characterized by significant small-scale density fluctuations, typically exhibit more pronounced small-scale filamentary structures. These morphological variations in integrated intensity maps of spectroscopic observations have been previously noted (Xu et al. 2019; Hu et al. 2019; Beattie & Federrath 2019). Earlier work by Peek & Burkhart (2019) and Hu et al. (2024) has demonstrated that Convolutional Neural Networks (CNNs; Lecun et al. 1998) are effective in extracting morphological features from spectroscopic observations and correlating these features with the M_A . Our current research builds on this foundation, marking the first attempt to use CNNs combined with spectroscopic observations to estimate M_s .

Moreover, the CNN approach extends beyond analyzing integrated intensity or column density maps. It also includes the examination of velocity centroid maps and

velocity channels (Lazarian & Pogosyan 2000; Kandel et al. 2016; Yuen et al. 2021; Hu et al. 2023), which offer additional insights into M_s based on velocity information (Yuen & Lazarian 2020). Applying CNNs to H I observations, particularly when combined with the velocity and spatial information provided by the Galactic rotation curve, enables modeling the 3D distribution of M_s across the Milky Way (Hu & Lazarian 2023). In this work, we train our CNN with synthetic spectroscopic observations generated from 3D simulations of MHD turbulence. We will compare the effectiveness of using intensity, centroid, and channel maps to estimate M_s .

This work is organized into five sections. § 2 describes the numerical MHD simulations, synthetic spectroscopic observations, and training strategies of the CNN. § 3 details the results of the CNN approach at predicting M_s numbers, including testing the effects of noise, magnetic field inclination, and missing low-spatial frequencies. § 4 discusses our results and their implications, and finally § 5 concludes our paper and provides future outlooks of this research.

2. NUMERICAL METHODS

2.1. MHD simulations

This study utilized MHD simulations which were generated from ZEUS-MP/3D (Hayes et al. 2006). We solve the ideal MHD equations in an Eulerian framework with associated periodic boundary and isothermal conditions. The simulation is regularly gridded into 512^3 cells.

The scale-free simulation of MHD turbulence can be characterized via the sonic Mach number $M_s = \delta v_{\text{inj}}/c_s$ and Alfvénic Mach number $M_A = \delta v_{\text{inj}}/v_A$, where v_{inj} is the turbulent velocity at injection scale, c_s is the sound speed, and v_A is the Alfvén speed. Initially, a uniform density field and magnetic field are set up and the magnetic field orientates perpendicular to the LOS. For this work, simulations were chosen based on having similar M_A values but different M_s values to feed the CNN with different turbulence conditions.

Turbulence is solenoidally driven at wavenumber $k = 2$ to achieve a Kolmogorov spectrum. We change the injection velocity v_{inj} to produce a wide variety of M_s values, as listed in Tab. 1. Similar MHD simulations have been used in Hu & Lazarian (2024a). We refer readers to Hu & Lazarian (2024a) for more details on the simulation.

2.2. Intensity, centroid, and channel maps

To create synthetic spectroscopic observations conducive to our CNN training, we utilize velocity and density fields derived from MHD simulations to con-

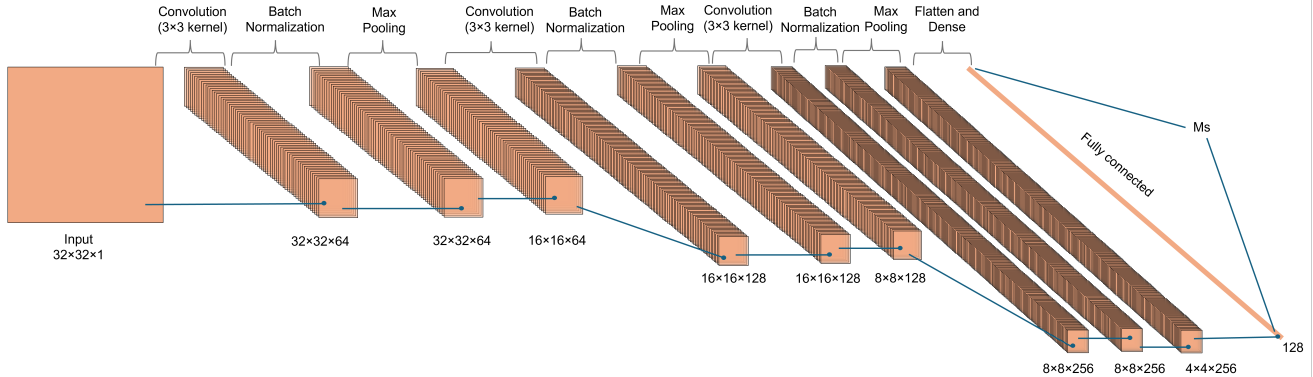


Figure 1. CNN model architecture utilized in this study. The input image is a 32×32 cells map cropped from either a channel, centroid, or intensity map. The CNN model then outputs a prediction of the sonic Mach numbers M_s .

Simulation	M_s	M_A	Range of M_s^{sub}
min01	2.17	0.51	1.36 - 2.84
min02	4.35	0.52	2.78 - 6.32
min03	6.53	0.52	3.85 - 8.97
min04	8.55	0.51	5.07 - 11.46
min05	10.86	0.69	6.18 - 13.68
min06	11.02	0.43	7.11 - 15.60

Table 1. M_s and M_A are the sonic Mach number and the Alfvénic Mach number calculated from the global injection velocity, respectively. M_s^{sub} values are determined using the local velocity dispersion calculated along each LOS in a 32×32 cells sub-field.

struct Position-Position-Velocity (PPV) cubes. From these PPV cubes, we generate intensity maps, velocity centroids, and velocity channel maps, each serving distinct purposes in our model training process.

Intensity maps are produced by fully integrating the PPV cubes along the LOS. This integration eliminates all velocity information, yielding a map that reflects only the density or intensity distribution. The intensity map, $I(x, y)$, is defined mathematically as:

$$I(x, y) = \int \rho(x, y, v_{\text{los}}) dv_{\text{los}}, \quad (1)$$

where $\rho(x, y, v_{\text{los}})$ represents the intensity values within the PPV cube, and v_{los} is the LOS velocity. $\rho(x, y, v_{\text{los}})$ corresponds to brightness or antenna temperature in observation.

Velocity centroids, $C(x, y)$, provide an intensity-weighted average velocity for each cell in the map, integrated along the LOS. They are calculated from:

$$C(x, y) = \frac{\int \rho(x, y, v_{\text{los}}) v_{\text{los}} dv_{\text{los}}}{\int \rho(x, y, v_{\text{los}}) dv_{\text{los}}}. \quad (2)$$

Velocity channel maps, $Ch(x, y)$, are derived by integrating the PPV cube over a narrowly defined velocity range. Unlike intensity maps, these channel maps are predominantly affected by velocity fluctuations due to the phenomenon known as velocity caustics (Lazarian & Pogosyan 2000; Kandel et al. 2016; Yuen et al. 2021; Hu et al. 2023). This effect arises when gas at different LOS positions but with similar LOS velocities is sampled into the same location in PPV space, leading to crowded and morphologically distorted intensity distributions.

The expression for a thin velocity channel is given by:

$$Ch(x, y) = \int_{v_0 - \Delta v/2}^{v_0 + \Delta v/2} \rho(x, y, v_{\text{los}}) dv_{\text{los}}, \quad (3)$$

where v_0 is the center velocity of the channel and Δv is the channel width, which is chosen to be less than the square root of the turbulence velocity dispersion, $\Delta v < \sqrt{(\delta v)^2}$.

These three maps have different weights of density and velocity information. We explore and compare them in terms of estimating M_s with the CNN model.

2.3. Convolutional Neural Network (CNN)

In this work, we adopt a CNN model to estimate M_s . The CNN model has been successfully applied to spectroscopic observation and radio observation to estimate M_A (Hu et al. 2024; Hu & Lazarian 2024a,b; Zhang et al. 2024). The CNN architecture consists of initial layers that stack on top of each other and make up convolution layers. This is then followed by pooling layers, in our case max pooling. Batch normalization layers follow each convolution layer and these layers help induce faster convergence during the training process. A prediction can be extracted and processed by the fully connected layers and outputs a prediction of the sonic Mach number. This CNN model is given in Fig. 1.

The target for training was the M_s . We use the Mean-Squared Error (MSE) loss function for backpropagation. For each training iteration, approximately 0.6 million sub-fields were used. We conducted at least 20 training iterations, continuing until the MSE loss function indicated saturation, suggesting that the model parameters had converged effectively.

2.4. Synthetic M_s maps

Our training input is either the intensity map, velocity centroid map, or velocity channel map generated from the simulations. The input maps are normalized by their maximum values so only morphological features in the map are the most important. For each 32×32 -cells sub-field, we also generate corresponding M_s^{sub} maps as per the following:

$$M_s^{\text{sub}} = \frac{v_{\text{inj}}^{\text{sub}}}{c_s}, \quad (4)$$

where M_s^{sub} is defined using the local velocity dispersion for each sub-field (i.e., $v_{\text{inj}}^{\text{sub}}$), rather than the global turbulent injection velocity v_{inj} used to characterize the full simulation. The ranges of M_s^{sub} averaged over the sub-field in each simulation are listed in Tab. 1. These values of M_s^{sub} cover typical physical conditions of the ISM.

2.5. Network training

The CNN’s trainable parameters undergo optimization by following a typical neural network training approach.

Random cropping: While training the CNN, we apply a strategy that helps with diversifying the training dataset which improves the generalization ability of the CNN. This strategy works by altering input images or data by applying random cropping to them which results in cell sizes of 32×32 (Takahashi et al. 2020). This random cropping method incorporates variability and randomness into the training data (Hu et al. 2024; Hu & Lazarian 2024a,b).

Random rotation: Another strategy employed in this work is the use of random rotations. Images that are utilized to train the model lack rotational invariance. In the CNN’s view, each cell is directly related to an element in a matrix. By rotating the image, the matrix’s elements are rearranged and create a new image for the model to train on (Larochelle et al. 2007). This fact can be utilized in two ways. The first is that by randomly rotating our 32×32 -cells, the training dataset can be further augmented. The second is that the original non-rotated datasets can be used as validation and a method of creating prediction test scenarios. In effect, random rotation enhances the training data with more diversity

and randomness to improve the accuracy of the CNN’s predictive capabilities across a wide variety of physical situations in the ISM (van Dyk & Meng 2001).

3. RESULTS

3.1. Intensity, centroid, and channel maps with different M_s

Fig. 2 presents three examples of intensity, velocity centroid, and velocity channel maps for different sonic Mach numbers, $M_s = 2.17, 4.35,$ and 6.53 , while maintaining similar Alfvénic Mach numbers, M_A . The intensity maps clearly show that intensity structures undergo significant changes as M_s increases. At a low M_s value of 2.17, intensity fluctuations are primarily concentrated on large scales due to the relatively weak influence of shocks. Their statistics are passively regulated by those of velocity fluctuations (Beresnyak et al. 2005). The resulting intensity structures tend to form coherent, large-scale filamentary patterns. However, as M_s increases, the impact of shocks becomes more pronounced, generating more small-scale, high-intensity fluctuations. This is particularly evident in the intensity map for $M_s = 6.53$, where the intensity structure shifts towards smaller-scale filamentary features. One could expect a large aspect ratio (width to height) of those structures in a high M_s medium. These results suggest that variations in M_s are distinctly imprinted on the intensity maps.

In the case of centroid maps, similar trends with varying M_s are observed. Compared to intensity maps, centroid maps incorporate intensity-weighted velocity information. At low M_s , the statistical behavior of velocity fluctuations closely resembles that of density fluctuations (Beresnyak et al. 2005), resulting in centroid structures that are morphologically similar to intensity structures. As M_s increases, small-scale fluctuations also become more prominent, though to a lesser extent than in the intensity maps. This is expected, as shocks tend to dissipate small-scale velocity fluctuations, leading to a steep velocity spectrum with a slope of approximately -2. Although centroid maps primarily reflect velocity information, the intensity weighting introduces some dependency on intensity, causing the structures to be influenced by changes in M_s .

In contrast, structures in channel maps are much less sensitive to variations in M_s . Regardless of the increase in M_s , channel maps consistently display highly filamentary small-scale structures. This behavior is primarily due to the dominance of velocity caustics in thin velocity channels (Lazarian & Pogosyan 2000; Kandel et al. 2016; Yuen et al. 2021; Hu et al. 2023). The statistics of these maps are therefore primarily governed by veloc-

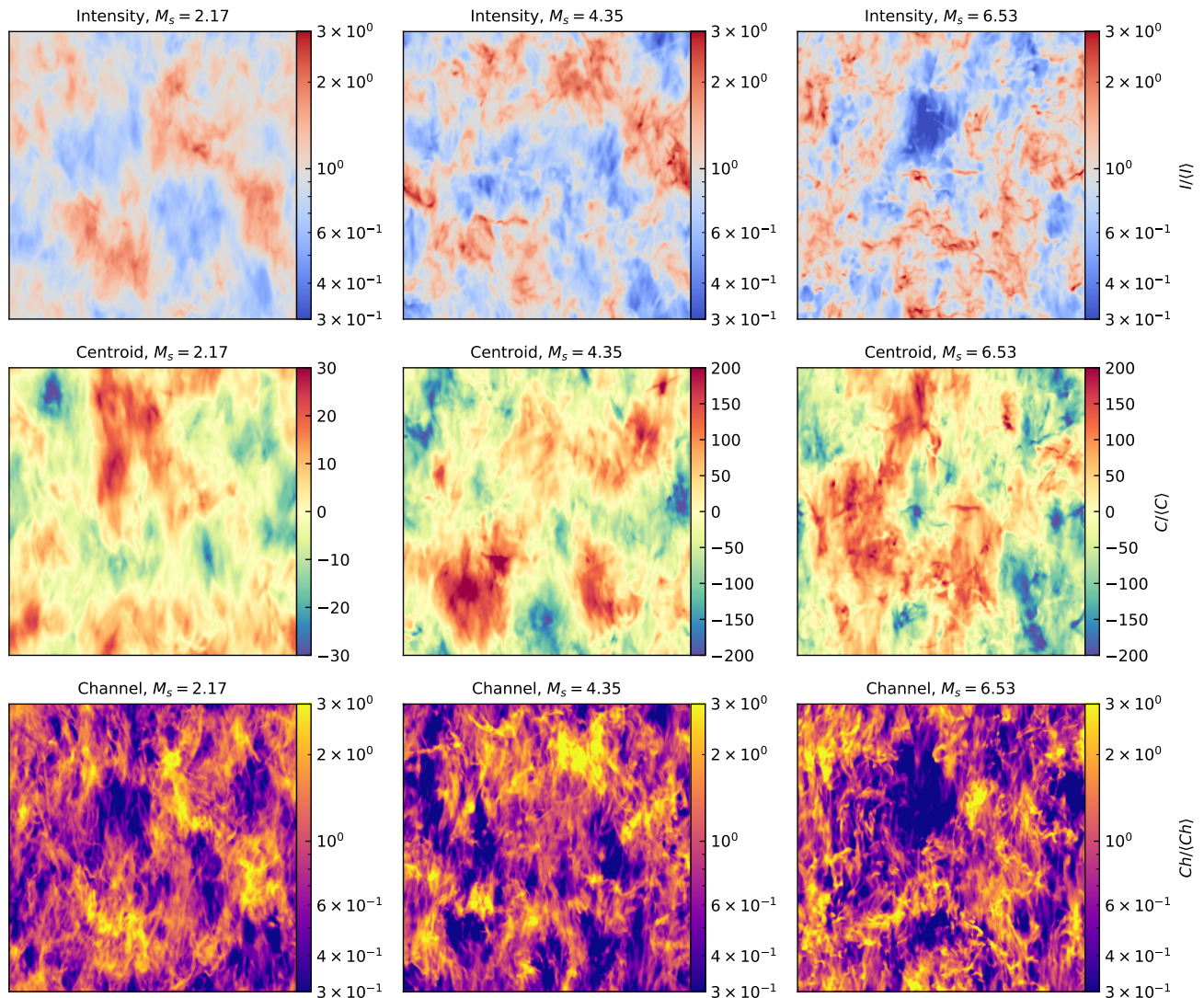


Figure 2. Maps of the integrated intensity (top), velocity centroid (middle), and thin velocity channel (bottom). Three simulations with different $M_s = 2.17, 4.35,$ and 6.53 are given here for comparison. From left to right M_s is increasing.

ity fluctuations, though density fluctuations also contribute. Compared to intensity and centroid maps, thin channel maps exhibit less sensitivity to changes in M_s .

3.2. Sonic Mach Number Predictions

Fig. 3 presents a comparison between the CNN-predicted sonic Mach number distribution, $M_{s,\text{CNN}}$, and the actual distribution, M_s^{sub} . The input to the CNN model is either an intensity map, centroid map, or channel map generated from the simulation $M_s = 11.02$. Overall, for all three kinds of input maps, their predicted $M_{s,\text{CNN}}$ distribution closely matches M_s^{sub} , although local discrepancies are present. Another example of predicting the $M_{s,\text{CNN}}$ in trans-/super-Alfvénic condition with $M_A = 1.07$ is given in Appendix A. The results are similar to these from sub-Alfvénic condition, suggesting

the CNN approach works for both strongly and weakly magnetized media.

Fig. 4 displays 2D histograms of $M_{s,\text{CNN}}$ and M_s^{sub} . Generally, for three kinds of input maps (intensity, centroid, and channel maps) the proximity of the data points to the one-to-one reference line indicates a statistical agreement between predicted and true values, highlighting the CNN model’s effectiveness, albeit with some scatter that reflects deviations from the actual values. The 2D histograms show that the CNN model overestimates for the low $M_s = 2.17$ case, while it is more likely to underestimate for the high $M_s = 11.02$ case.

3.3. Effect of the mean magnetic field’s inclination

The CNN approach for predicting the M_s distribution is based on the morphological changes in intensity,

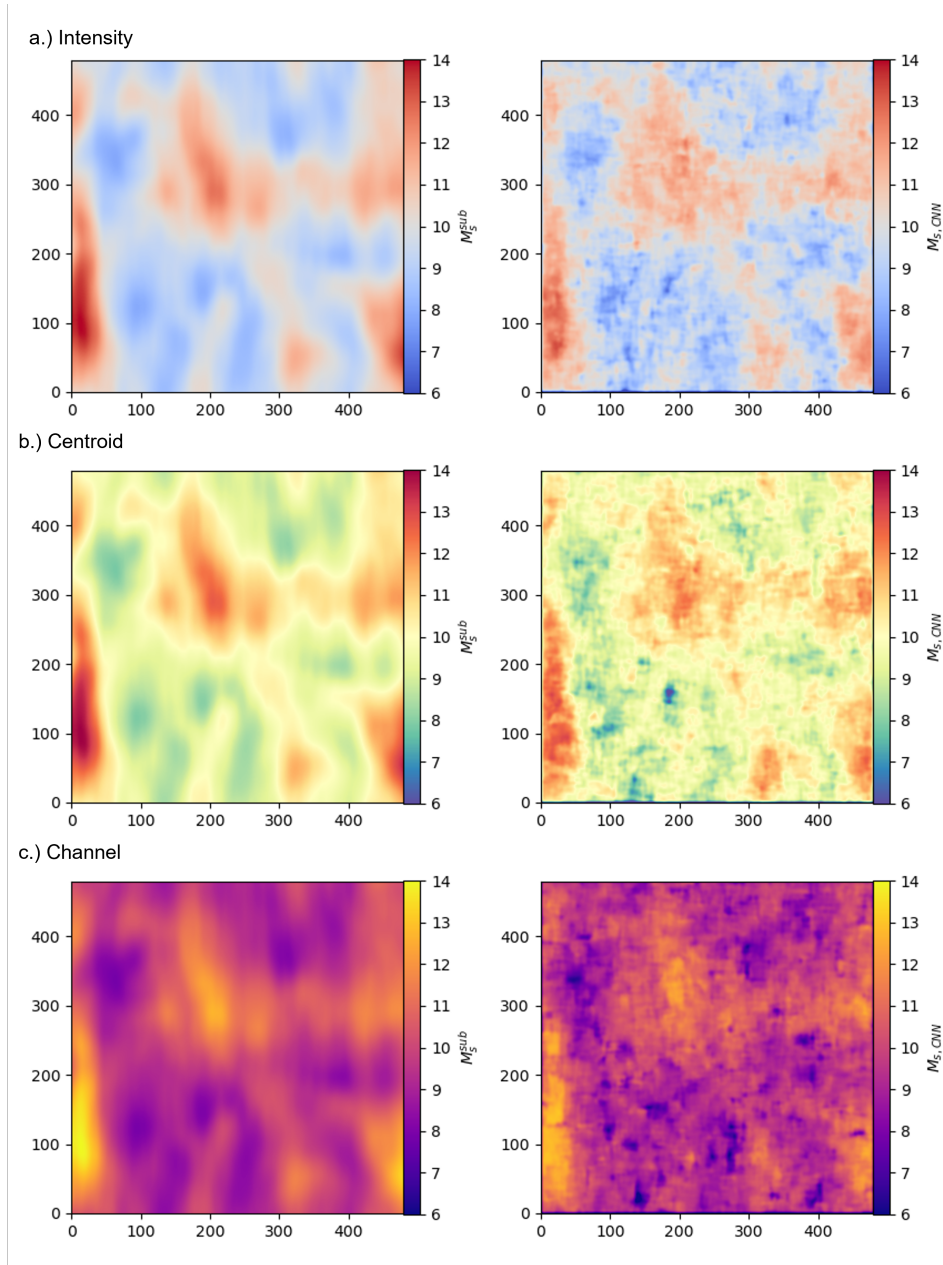


Figure 3. The right column presents a comparison of the CNN-predicted sonic Mach number $M_{s,CNN}$ distribution from intensity (top), centroid (middle), and channel input maps (bottom) and the actual M_s^{sub} distribution in the left column. The supersonic simulation with $M_s = 11.02$ is used as an example here.

centroid, and channel structures under varying M_s conditions. Another factor that may influence the observed structures is the inclination angle of the mean magnetic field. In a magnetized turbulent medium, density and velocity structures tend to elongate along magnetic fields in subsonic conditions, whereas, in the supersonic regime, small-scale density structures can become perpendicular to the magnetic fields due to shock effects (Hu et al. 2019; Xu et al. 2019). This elongation is a well-known consequence of the anisotropy of MHD turbulence (Goldreich & Sridhar 1995; Lazarian & Vishniac

1999). When the mean magnetic field is perpendicular to the LOS, this elongation is most pronounced, as shown in Fig. 2, where the mean magnetic field is aligned along the vertical axis. However, as the inclination angle between the mean magnetic field and the LOS decreases, the observed structures change. In particular, when the mean field is fully parallel to the LOS, the elongation effect cannot be observed.

To investigate the effect of the mean field’s inclination, we rotate the simulation boxes to achieve four different inclination angles (90, 60, 30, and 0 degrees),

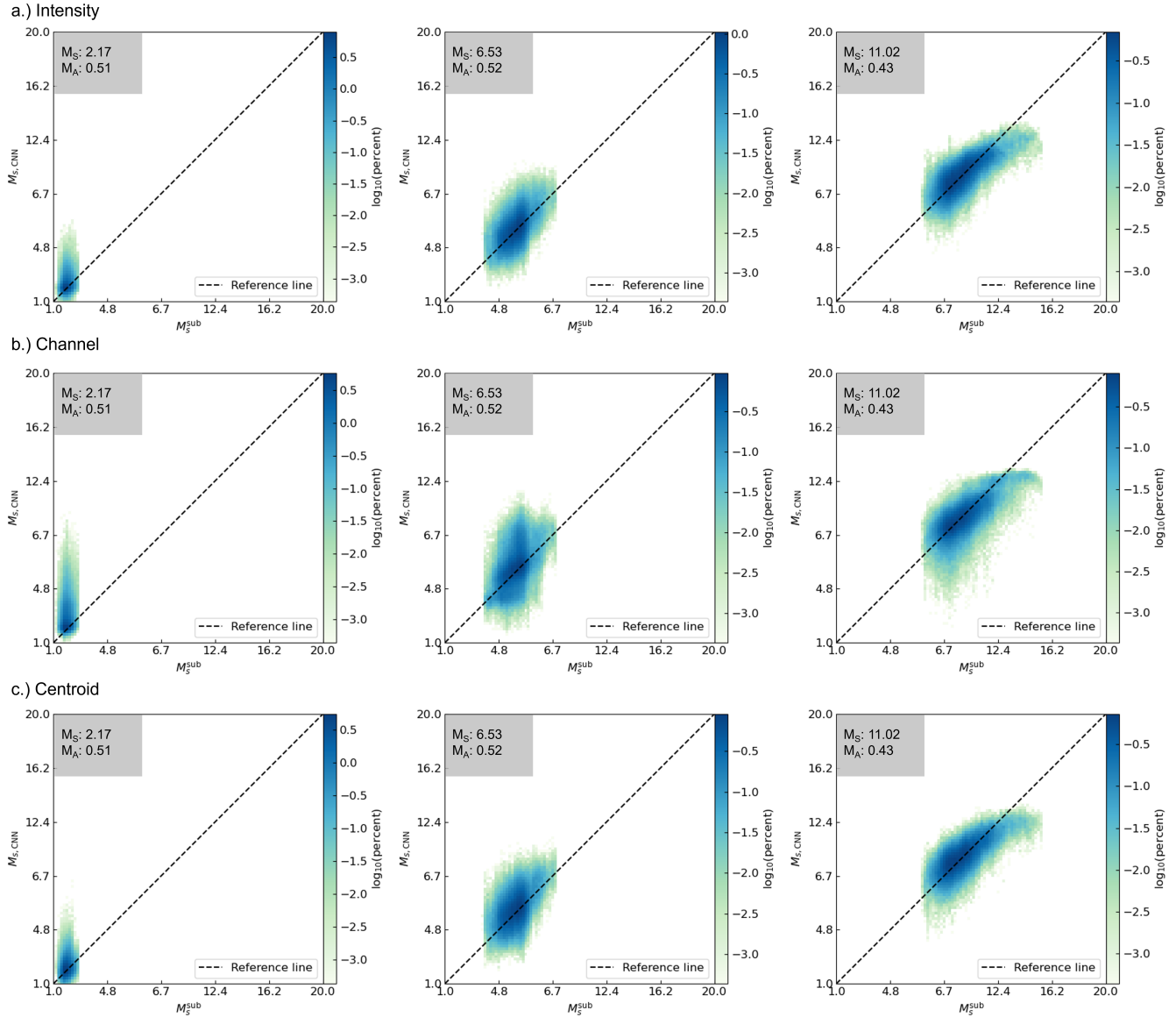


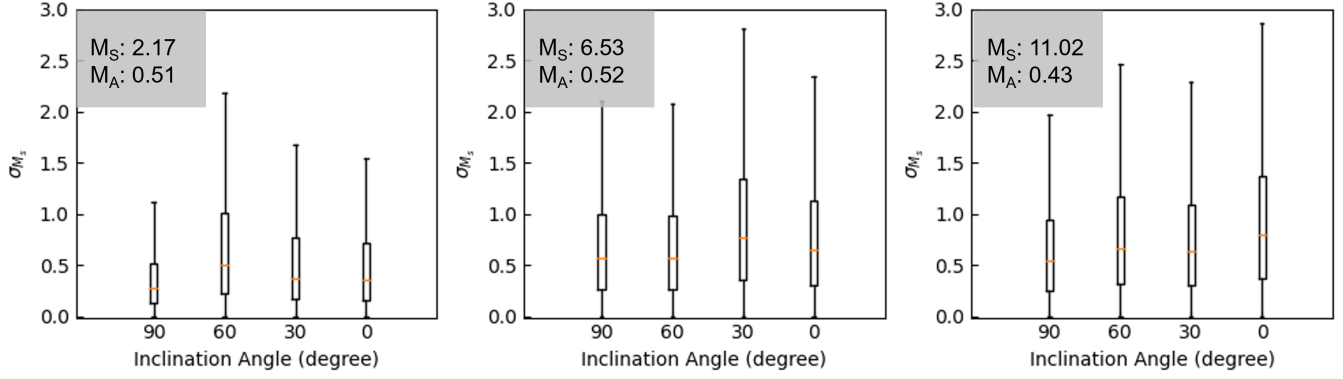
Figure 4. 2D histograms comparing CNN-predicted $M_{s,CNN}$ and actual M_s of three simulations $M_s = 2.17, 6.53,$ and 11.02 . $M_{s,CNN}$ is predicted from either intensity map (top), velocity channel map (middle), or centroid map (bottom). The dashed reference line refers to the one-to-one correlation.

generate synthetic spectroscopic data, and retrain the CNN model accordingly. We quantify the CNN prediction error by calculating the absolute difference between the predicted and actual M_s values, denoted as σ_{M_s} . Fig. 5 presents box plots of σ_{M_s} for three simulations with $M_s = 2.17, 6.53,$ and 11.02 , across the four inclination angles (90, 60, 30, and 0 degrees). This box plot analysis was conducted for all three types of input maps—intensity, centroid, and channel maps—used to make the predictions.

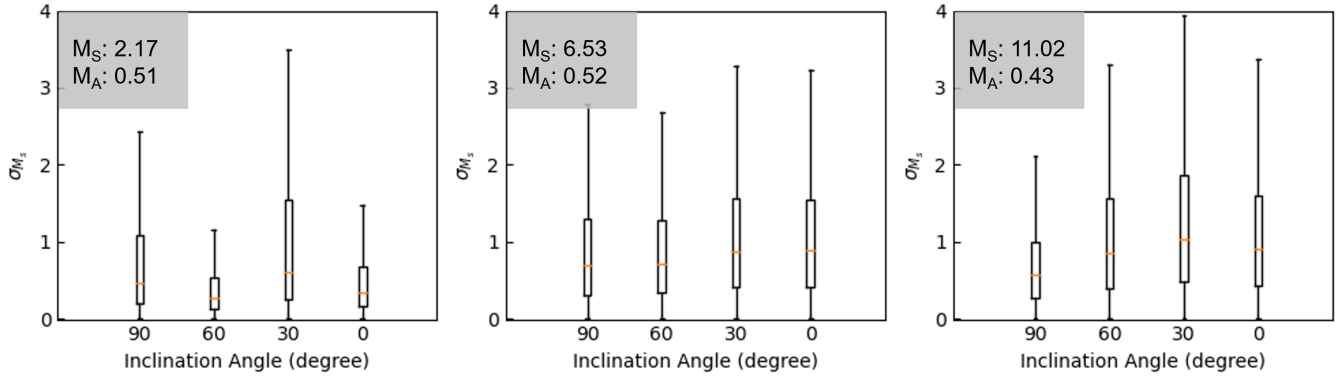
For predictions based on all three map types shown in Fig. 5, the median error is generally around 0.5 when the

inclination angle is 90 degrees, while for the $M_s = 2.17$ case, the median error is lower, ranging from 0.2 to 0.3. Although maximum or upper quartile error values vary more at higher M_s , the median error remains approximately $\sigma_{M_s} = 0.5$ across simulations with different M_s values. When comparing errors calculated from intensity, centroid, and channel maps, while their median errors are similar, the maximum and upper quartile error values tend to be lowest for intensity maps and highest for channel maps, especially for the lower $M_s = 2.17$ and $M_s = 6.53$ cases.

a.) Intensity



b.) Channel



c.) Centroid

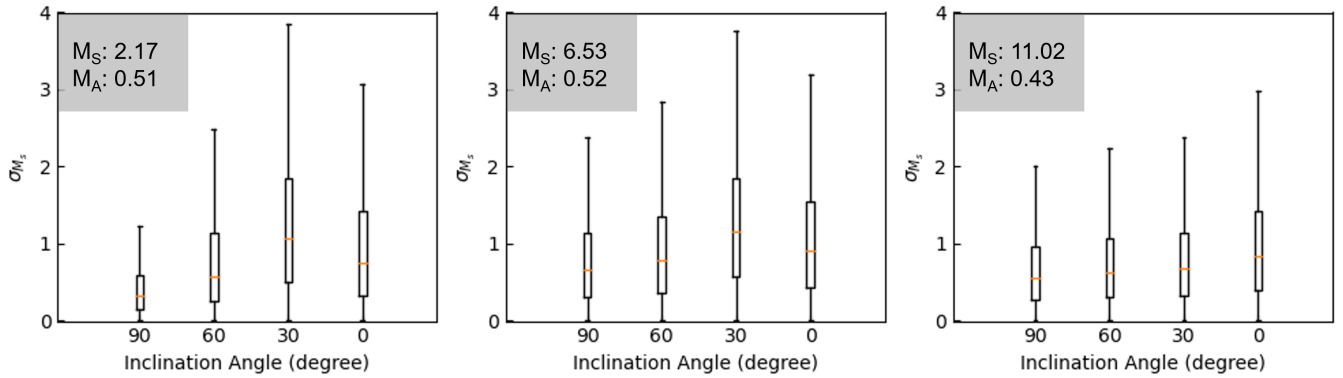


Figure 5. Box plots of the absolute difference σ_{M_s} between CNN-predicted M_s and actual M_s^{sub} values for various inclination angles of mean magnetic field. Three simulations $M_s = 2.17, 6.53,$ and 11.02 are used. $M_{s,\text{CNN}}$ is predicted from either intensity map (top), velocity channel map (middle), or centroid map (bottom). The box provides the range of the first quartile (lower) to the third quartile (upper), the upper and lower line gives the maximum and minimum error respectively, and the orange line represents the median value.

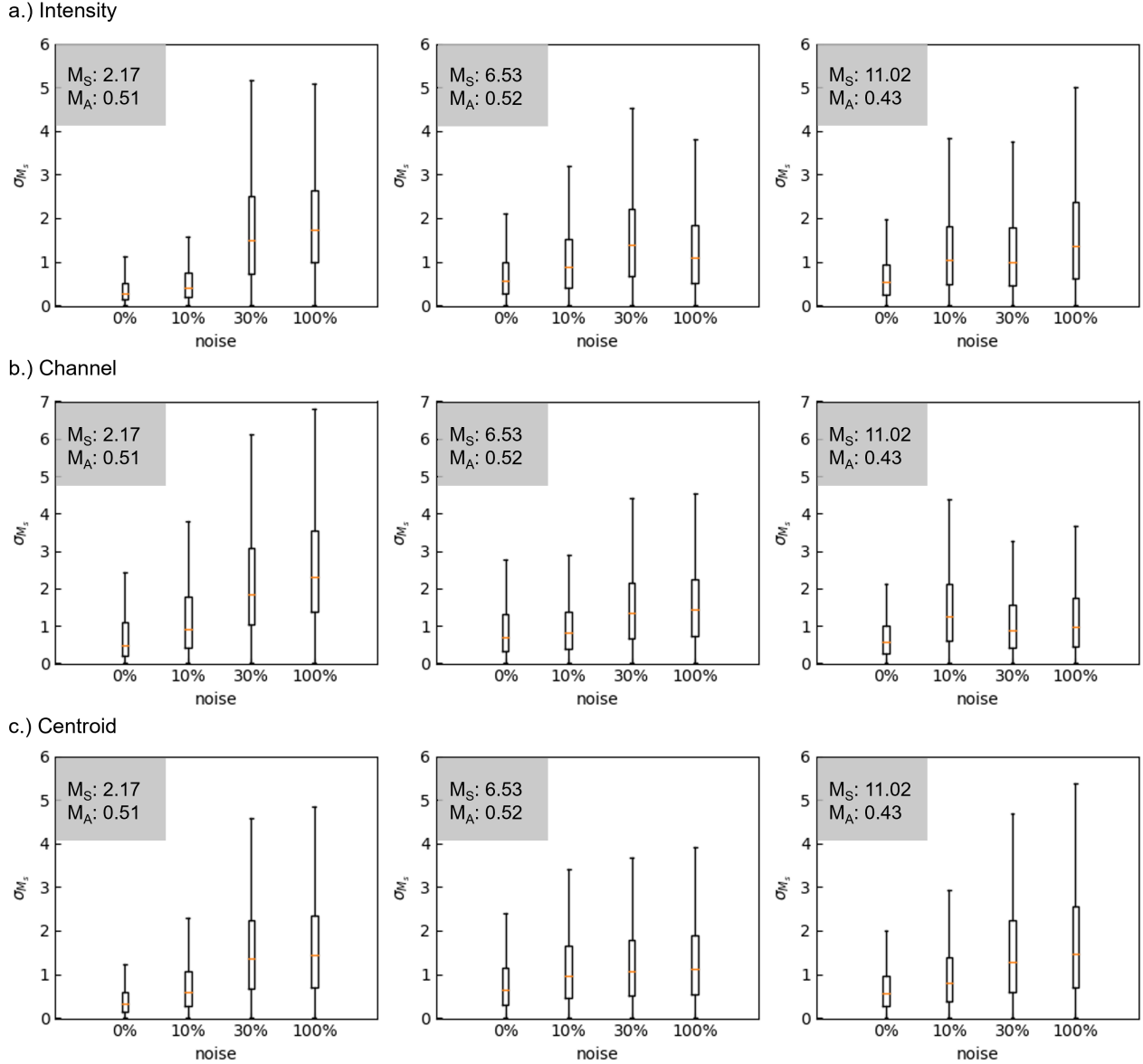
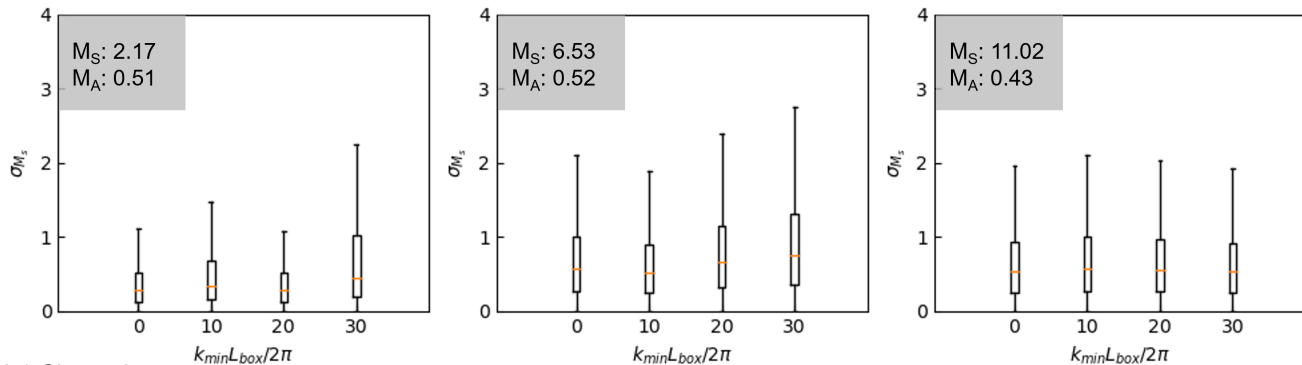
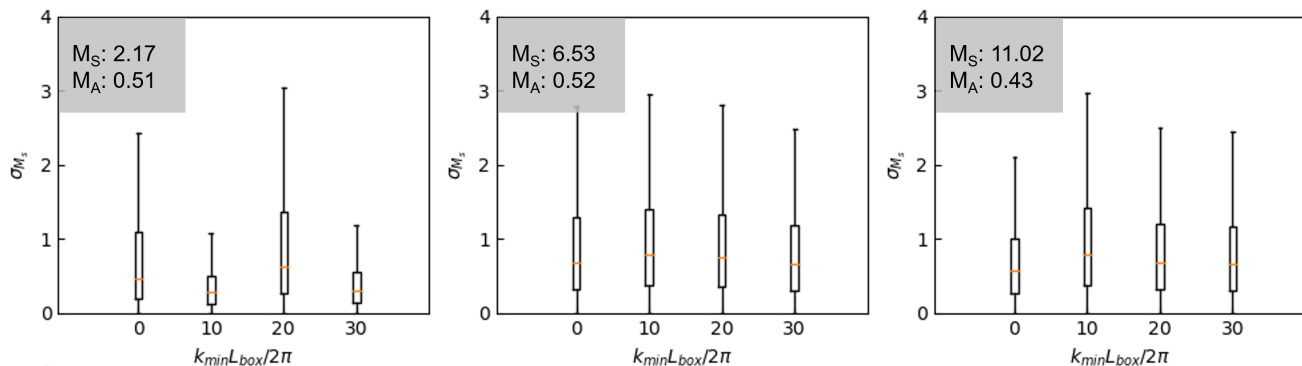


Figure 6. Box plots of the absolute difference σ_{M_s} between CNN-predicted M_s and actual M_s^{sub} values for various levels of noise. Three simulations $M_s = 2.17, 6.53,$ and 11.02 with an inclination angle of 90 degrees are used. $M_{s,\text{CNN}}$ is predicted from either intensity map (top), velocity channel map (middle), or centroid map (bottom). The box provides the range of the first quartile (lower) to the third quartile (upper), the upper and lower line gives the maximum and minimum error respectively, and the orange line represents the median value.

a.) Intensity



b.) Channel



c.) Centroid

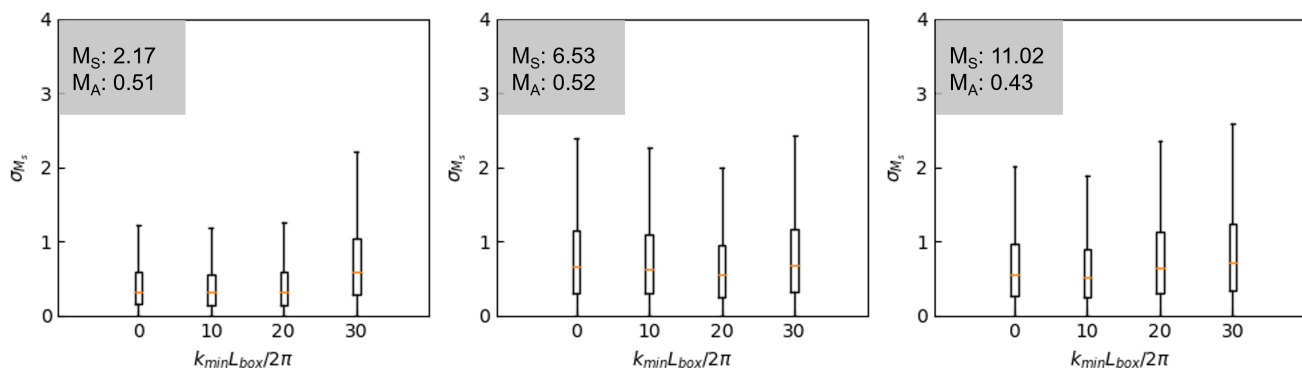


Figure 7. Box plots of the absolute difference σ_{M_s} between CNN-predicted M_s and actual M_s^{sub} values for various levels of removed spatial frequencies. K_{\min} represents minimum wavenumber remaining in the filtered input map and L_{box} is the size of simulation box. Each of the three simulations $M_s = 2.17, 6.53,$ and 11.02 were studied for the 90 degree inclination angle case. $M_{s,\text{CNN}}$ is predicted from either intensity map (top), velocity channel map (middle), or centroid map (bottom). The box provides a range of error from the first quartile (lower) to the third quartile (upper). The upper and lower line gives the maximum and minimum error respectively, and the orange line represents the median σ_{M_s} error value.

For the 60, 30, and 0 degrees inclination angles, where the magnetic field is not perpendicular to the LOS, the error exhibits more variations, with effectively higher maximum and upper quartile values. As seen in Fig. 5, as the inclination angle decreases from 90 to 0 degrees, the error σ_{M_s} generally increases. This is particularly evident for predictions from channel maps, where the error is highest for the 0 degrees and 30 degrees cases. In contrast, predictions from intensity maps appear less sensitive to the inclination angle. Nevertheless, the median errors remain generally below 0.75 across all inclination angles, highlighting the robustness of our CNN architecture in accurately predicting M_s values.

3.4. Noise effect

Noise is unavoidable in observation and may diminish useful information in the intensity, centroid, and channel maps. In this section, we examine the impact of noise on our CNN model’s performance. We introduce Gaussian noise to the maps, with the noise level quantified by the noise ratio (NR), defined as the ratio of the Gaussian noise’s standard deviation to the mean value of the intensity, channel, or centroid maps.

Fig. 5 presents the absolute error σ_{M_s} for three simulations with $M_s = 2.17$, 6.53, and 11.02 across four different NR values: 0%, 10%, 30%, and 100%. This analysis is conducted for three types of input maps—intensity, centroid, and channel maps, all with an inclination angle of 90 degrees—on which the CNN model is trained to make predictions. In the noise-free case, the median error remains low, with the 0% NR median σ_{M_s} values staying below 0.75 for all input maps. The results for the 0% NR case, which corresponds to the 90-degree case for each input map, were discussed in the previous section. Across all input map types and M_s values, the median error remains generally below 2, despite increasing with rising noise levels.

In simulations with added noise (NR values of 10%, 30%, and 100%), the error increases relative to the noise-free case. Across all input map types and M_s values, the median σ_{M_s} values rise as the noise ratio increases. In addition to the median errors, the upper quartile values also increase, with the largest errors occurring in the 30% and 100% NR simulations for all map types. For intensity maps, the highest median error occurs for the $M_s = 2.17$ case at 100% NR, though similarly high values are observed for the $M_s = 6.53$ case at 30% NR and the $M_s = 11.02$ case at 100% NR. Notably, for intensity maps, the median σ_{M_s} never exceeds 2 in any of the noise-added simulations.

For channel maps, $M_s = 2.17$ shows the highest median and upper quartile σ_{M_s} values, with σ_{M_s} exceeding

2 in the 100% NR case and approaching 2 in the 30% NR case. The $M_s = 11.02$ case for channel maps displays the highest median error for the 10% NR model across all input map types and M_s values. However, for both $M_s = 6.53$ and $M_s = 11.02$, the median σ_{M_s} values generally remain below 2 for all map types. For centroid maps, the trend of increasing median σ_{M_s} with rising noise levels persists. Although the 100% NR models for all three M_s values show the highest error values, these errors remain below 2.

The effectiveness of our CNN model in accurately predicting M_s values is evidenced by the consistently low median σ_{M_s} across all input map types and noise conditions. As expected, increased noise levels generally led to higher median and upper-quartile error values. Specifically, the median errors rose from less than 0.75 in the noise-free cases to approximately 2 – 2.25 under the highest noise conditions. These increases make predictions more challenging for lower M_s values, such as in our simulation with $M_s = 2.17$. However, for higher M_s values, such as $M_s > 10$, a median error of around 2, even in the presence of 100% noise, remains relatively favorable.

3.5. Removal of Lower Spatial Frequencies

For extra-galactic spectroscopic observations, telescope arrays like the Very Large Array (VLA) are often used. Due to limited baselines, these observations are usually constrained by the loss of low spatial frequencies which are necessary to resolve large-scale features of structures within images. In this study, we tested our CNN model’s predictive ability when lower spatial frequencies are removed. We applied a k -space filter to the intensity, centroid, and channel maps before CNN training, following these steps: (i) performing a Fast Fourier Transform (FFT) on the 2D map, (ii) filtering out intensity values from wavenumber $k = 0$ to k_{\min} to emphasize high-spatial frequencies, and (iii) applying an inverse FFT to transform the filtered map back into the spatial domain. We explored four different ranges of removed spatial frequencies—0, 0 - 10, 0 - 20, and 0 - 30—across three different M_s simulations for each of the three input map types.

Fig. 7 presents box plots of the prediction error corresponding to the different input maps, M_s simulations, and removed spatial frequency ranges used for CNN model training. Across all input map types, the median error is less than one, as shown in Fig. 7. There is a general trend of increasing median and upper quartile error values as more spatial frequencies are removed, particularly for the intensity and centroid input maps.

However, the channel input maps exhibit some irregularities in this trend.

For the intensity input maps, the $M_s = 2.17$ simulation shows the lowest overall median error, with values below 0.5. As more spatial frequencies are removed, the prediction error increases, reaching its highest maximum error for the 0 - 30 spatial frequency removal case. Despite this, the median σ_{M_s} remains below one. As higher M_s simulations are used for training, there is an increase in median σ_{M_s} values. The $M_s = 11.02$ simulation shows an almost constant median error across all spatial frequency regimes, with values consistently below one.

In the centroid input map case, the median σ_{M_s} remains stably below one, with a general trend of increasing σ_{M_s} as the simulation regime transitions from low M_s to high M_s . The $M_s = 2.17$ simulation shows the lowest errors, with the 0 - 10 and 0 - 20 removed spatial frequency cases producing σ_{M_s} values below 0.5. Both $M_s = 6.53$ and $M_s = 11.02$ display similar median σ_{M_s} values, ranging between 0.5 and one across all removed spatial frequency instances.

In the channel input map predictions, more erratic behavior is observed. Unlike the intensity and centroid maps, no consistent trend emerges across the three M_s simulations, with higher median and maximum σ_{M_s} values recorded. The $M_s = 2.17$ simulation still demonstrates the lowest error values, although the 0 - 20 spatial frequency removal case shows a median error exceeding 0.5 but remains below one. For the $M_s = 6.53$ and $M_s = 11.02$ simulations, the predictions reveal an almost inverse trend compared to other training scenarios, where the median and upper quartile σ_{M_s} values decrease as the minimum retained spatial frequency increases. Despite this irregularity, the median error values for both simulations consistently remain below one. Across all three input map types and for all M_s simulations, the error values stay below one—even when the largest amount of spatial frequencies is removed. This highlights the robustness of our CNN model in predicting M_s using interferometric observations.

4. DISCUSSION

4.1. Comparison with other methods

In this study, we trained a CNN model to predict M_s using spectroscopic observations. The CNN approach offers several advantages over traditional methods, which typically rely on the statistics of density fluctuations. The CNN model can be applied to velocity channel maps, suggesting the potential to map M_s 3D distribution by combining velocity information from spectroscopic observations with the Galactic rotation

curve. Additionally, the ability to accurately measure M_s under conditions where lower spatial frequencies are removed is crucial for applications involving interferometric data. As demonstrated, our model performs well in noisy environments and when low spatial frequencies are unavailable. Furthermore, the CNN model is trained using numerical simulations. While turbulence simulations were employed in this study, more complex simulations may be required for additional physical processes, such as gravitational collapse and outflow feedback, in the targeted clouds.

4.2. Measuring magnetic field strength in molecular cloud

The magnetic field strength is crucial for understanding the role magnetic fields play in star formation (Mestel & Spitzer 1956; Mestel 1966; Mac Low & Klessen 2004; McKee & Ostriker 2007; Crutcher 2012). The CNN approach is particularly advantageous due to its flexibility in providing crucial parameters for measuring the magnetic field strength in molecular clouds. Previous research has demonstrated that CNN models can successfully predict the M_A (Hu et al. 2024). The two Mach numbers can be combined synergistically to estimate the magnetic field strength using the following relation (Lazarian et al. 2020; Hu & Lazarian 2023):

$$B = c_s \sqrt{4\pi\rho} M_s M_A^{-1}, \quad (5)$$

where B is the magnetic field strength, c_s is the sound speed, and ρ is the gas mass density. Thus, assuming c_s is approximately constant in an isothermal molecular cloud, one could combine M_A and M_s to measure the spatial distribution of the total magnetic field strength.

4.3. Measuring 3D Galactic Magnetic Field strength

Determination of the 3D Galactic magnetic field is vital to understanding many astrophysical processes and our own Galaxy, including the origin of ultra-high-energy cosmic rays (Yan & Lazarian 2002; Beattie et al. 2022; Lazarian & Xu 2023) and the modeling of foreground polarization for the CMB B-mode polarization detection (Kovetz & Kamionkowski 2015; Planck Collaboration: et al. 2015).

Recently, research conducted has shown thin channel maps can be used synergistically with the Galactic rotational curve to map the 3D GMF (Lazarian & Yuen 2018; Hu et al. 2023; Schmaltz et al. 2024). Intensity and velocity centroid maps are only able to map 2D POS magnetic fields. This makes channel input maps the ideal candidate for training CNN models to predict the 3D M_s distribution, as well as the 3D GMF strength, based on Eq. 5.

In addition, our CNN model demonstrated strong predictive capabilities, as evidenced by median σ_{M_s} values consistently measured below 1 across all simulations when low spatial frequencies were removed. Given this success, magnetic field strength measurements could be extended extragalactically using high-resolution interferometric observation.

4.4. Understanding the compressibility of turbulence in ISM

The information of M_s is important in determining the gas compressibility $\beta = 2(M_A/M_s)^2$. This compressibility is a key factor in understanding the fragmentation of molecular clouds, turbulent support, and the acceleration and diffusion of cosmic rays. In low-beta environments, where magnetic pressure dominates, magnetic fields play a significant role in shaping the gas dynamics. This can lead to higher gas compression in shocks and more efficient fragmentation of molecular clouds, facilitating the formation of dense structures and accelerating gravitational collapse, which increases the star formation efficiency (Mestel & Spitzer 1956; Mestel 1966; Mac Low & Klessen 2004). On the other hand, the strong magnetic fields restrict cosmic ray motion in the direction perpendicular to the magnetic field, resulting in a smaller perpendicular diffusion coefficient (Yan & Lazarian 2008; Xu & Yan 2013; Hu et al. 2022a).

5. CONCLUSION

In conclusion, this study demonstrates the successful application of Convolutional Neural Networks (CNNs) in estimating the sonic Mach number M_s of the ISM from spectroscopic data. The underlying physical principle of the CNN approach is that morphological changes in density and intensity structures are indicative of varying M_s values. In highly supersonic media, characterized by significant small-scale density fluctuations, more pronounced small-scale filamentary structures are typically observed. By utilizing intensity, centroid, or velocity channel maps, the CNN effectively captures these structural changes, enabling accurate predictions of M_s across diverse turbulence conditions, noise levels, and magnetic field inclinations. The CNN model's robustness, even under observational constraints such as the absence of low spatial frequencies, underscores its potential for analyzing interferometric data.

1 T.S. and A.L. acknowledge the support of NSF grants
 2 AST 2307840, and ALMA SOSPADA-016. Y.H. ac-
 3 knowledges the support for this work provided by NASA
 4 through the NASA Hubble Fellowship grant # HST-
 5 HF2-51557.001 awarded by the Space Telescope Sci-
 6 ence Institute, which is operated by the Association
 7 of Universities for Research in Astronomy, Incorpo-
 8 rated, under NASA contract NAS5-26555. This work
 9 used SDSC Expanse CPU, NCSA Delta CPU, and
 10 NCSA Delta GPU through allocations PHY230032,
 11 PHY230033, PHY230091, PHY230105, and PHY240183
 12 from the Advanced Cyberinfrastructure Coordination
 13 Ecosystem: Services & Support (ACCESS) program,
 14 which is supported by National Science Foundation
 15 grants #2138259, #2138286, #2138307, #2137603, and
 16 #2138296.

Software: Python3 (Van Rossum & Drake 2009);
 TensorFlow (Abadi et al. 2015)

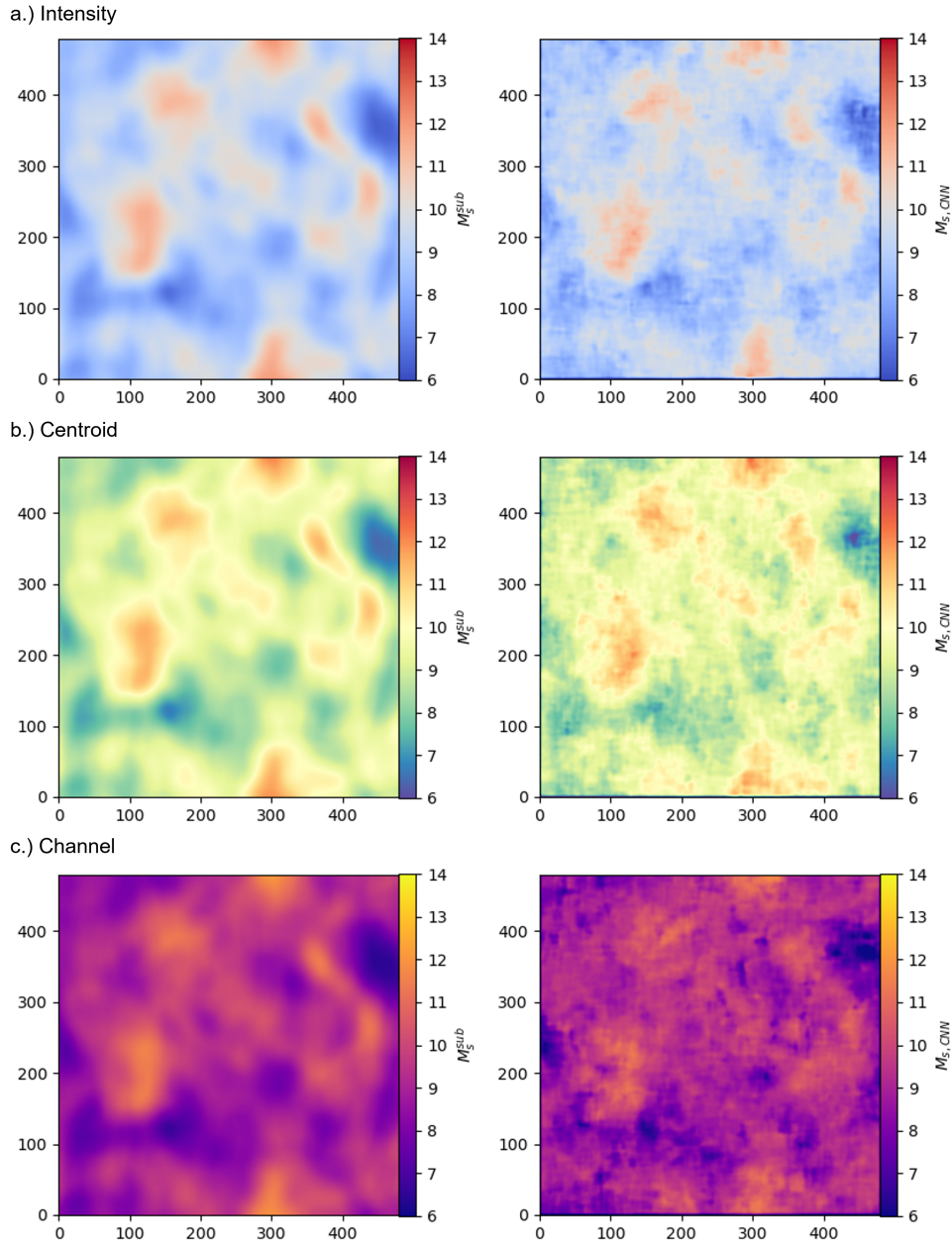


Figure 8. The right column presents a comparison of the CNN-predicted sonic Mach number $M_{s,CNN}$ distribution from intensity (top), centroid (middle), and channel input maps (bottom) and the actual M_s^{sub} distribution in the left column. The supersonic simulation with $M_s = 11.02$ and $M_A = 1.07$ is used as an example here.

APPENDIX

A. HIGH ALFVÉNIC MACH NUMBER SIMULATION EFFECT ON M_s PREDICTION

Figs. 8 displays the output of our CNN model when predicting sonic Mach numbers for a simulation with an associated higher Alfvénic Mach number, $M_A = 1.07$, than the other sub-Alfvénic simulations used in this work. The prediction shows similar M_s structures to the training map and demonstrates the robustness of our model to also train for varying Alfvénic Mach number situations in supersonic molecular clouds.

REFERENCES

- Abadi, M., Agarwal, A., Barham, P., et al. 2015, TensorFlow: Large-Scale Machine Learning on Heterogeneous Systems. <https://www.tensorflow.org/>
- Armstrong, J. W., Rickett, B. J., & Spangler, S. R. 1995, *ApJ*, 443, 209, doi: [10.1086/175515](https://doi.org/10.1086/175515)
- Ballesteros-Paredes, J., Vázquez-Semadeni, E., Gazol, A., et al. 2011, *MNRAS*, 416, 1436, doi: [10.1111/j.1365-2966.2011.19141.x](https://doi.org/10.1111/j.1365-2966.2011.19141.x)
- Beattie, J. R., & Federrath, C. 2019, *Monthly Notices of the Royal Astronomical Society*, 492, 668, doi: [10.1093/mnras/stz3377](https://doi.org/10.1093/mnras/stz3377)
- Beattie, J. R., Krumholz, M. R., Federrath, C., Sampson, M. L., & Crocker, R. M. 2022, *Frontiers in Astronomy and Space Sciences*, 9, doi: [10.3389/fspas.2022.900900](https://doi.org/10.3389/fspas.2022.900900)
- Beresnyak, A., Lazarian, A., & Cho, J. 2005, *ApJL*, 624, L93, doi: [10.1086/430702](https://doi.org/10.1086/430702)
- Berkhuijsen, E. M., & Fletcher, A. 2008, *Monthly Notices of the Royal Astronomical Society: Letters*, 390, L19, doi: [10.1111/j.1745-3933.2008.00526.x](https://doi.org/10.1111/j.1745-3933.2008.00526.x)
- Bracco, A., Ghosh, T., Boulanger, F., & Aumont, J. 2019, *Astronomy & Astrophysics*, 632, A17, doi: [10.1051/0004-6361/201935951](https://doi.org/10.1051/0004-6361/201935951)
- Brunt, C. M. 2010, *A&A*, 513, A67, doi: [10.1051/0004-6361/200913506](https://doi.org/10.1051/0004-6361/200913506)
- Burkhart, B. 2018, *ApJ*, 863, 118, doi: [10.3847/1538-4357/aad002](https://doi.org/10.3847/1538-4357/aad002)
- Burkhart, B., & Lazarian, A. 2012, *The Astrophysical Journal Letters*, 755, L19, doi: [10.1088/2041-8205/755/1/L19](https://doi.org/10.1088/2041-8205/755/1/L19)
- Burkhart, B., Stanimirović, S., Lazarian, A., & Kowal, G. 2009, *The Astrophysical Journal*, 708, 1204, doi: [10.1088/0004-637X/708/2/1204](https://doi.org/10.1088/0004-637X/708/2/1204)
- Chepurnov, A., & Lazarian, A. 2010, *ApJ*, 710, 853
- Crutcher, R. M. 2004, in *The Magnetized Interstellar Medium*, ed. B. Uyaniker, W. Reich, & R. Wielebinski, 123–132
- Crutcher, R. M. 2012, *ARA&A*, 50, 29, doi: [10.1146/annurev-astro-081811-125514](https://doi.org/10.1146/annurev-astro-081811-125514)
- Elmegreen, B. G. 1993, *ApJL*, 419, L29, doi: [10.1086/187129](https://doi.org/10.1086/187129)
- Esquivel, A., & Lazarian, A. 2010, *The Astrophysical Journal*, 710, 125, doi: [10.1088/0004-637X/710/1/125](https://doi.org/10.1088/0004-637X/710/1/125)
- Federrath, C., & Banerjee, S. 2015, *MNRAS*, 448, 3297, doi: [10.1093/mnras/stv180](https://doi.org/10.1093/mnras/stv180)
- Federrath, C., & Klessen, R. S. 2012, *ApJ*, 761, 156, doi: [10.1088/0004-637X/761/2/156](https://doi.org/10.1088/0004-637X/761/2/156)
- Federrath, C., Klessen, R. S., & Schmidt, W. 2008, *ApJL*, 688, L79, doi: [10.1086/595280](https://doi.org/10.1086/595280)
- Ghilea, M. C., Ruffolo, D., Chuychai, P., et al. 2011, *ApJ*, 741, 16, doi: [10.1088/0004-637X/741/1/16](https://doi.org/10.1088/0004-637X/741/1/16)
- Goldreich, P., & Sridhar, S. 1995, *ApJ*, 438, 763, doi: [10.1086/175121](https://doi.org/10.1086/175121)
- Ha, T., Li, Y., Kounkel, M., et al. 2022, *ApJ*, 934, 7, doi: [10.3847/1538-4357/ac76bf](https://doi.org/10.3847/1538-4357/ac76bf)
- Hayes, J. C., Norman, M. L., Fiedler, R. A., et al. 2006, *The Astrophysical Journal Supplement Series*, 165, 188, doi: [10.1086/504594](https://doi.org/10.1086/504594)
- Hill, A. S., Benjamin, R. A., Kowal, G., et al. 2008, *The Astrophysical Journal*, 686, 363, doi: [10.1086/590543](https://doi.org/10.1086/590543)
- Hu, Y., Federrath, C., Xu, S., & Mathew, S. S. 2022, *MNRAS*, 513, 2100, doi: [10.1093/mnras/stac972](https://doi.org/10.1093/mnras/stac972)
- Hu, Y., & Lazarian, A. 2023, *Monthly Notices of the Royal Astronomical Society*, 524, 2379–2394, doi: [10.1093/mnras/stad1996](https://doi.org/10.1093/mnras/stad1996)
- Hu, Y., & Lazarian, A. 2024a, arXiv e-prints, arXiv:2404.07806, doi: [10.48550/arXiv.2404.07806](https://doi.org/10.48550/arXiv.2404.07806)
- . 2024b, arXiv e-prints, arXiv:2410.09294, doi: [10.48550/arXiv.2410.09294](https://doi.org/10.48550/arXiv.2410.09294)
- Hu, Y., Lazarian, A., Alina, D., Pogosyan, D., & Ho, K. W. 2023, *MNRAS*, 524, 2994, doi: [10.1093/mnras/stad1924](https://doi.org/10.1093/mnras/stad1924)
- Hu, Y., Lazarian, A., Beck, R., & Xu, S. 2022, *The Astrophysical Journal*, 941, 92, doi: [10.3847/1538-4357/ac9df0](https://doi.org/10.3847/1538-4357/ac9df0)
- Hu, Y., Lazarian, A., & Stanimirović, S. 2021, *The Astrophysical Journal*, 912, 2, doi: [10.3847/1538-4357/abedb7](https://doi.org/10.3847/1538-4357/abedb7)
- Hu, Y., Lazarian, A., Wu, Y., & Fu, C. 2024, *MNRAS*, 527, 11240, doi: [10.1093/mnras/stad3766](https://doi.org/10.1093/mnras/stad3766)
- Hu, Y., Lazarian, A., & Xu, S. 2022a, *MNRAS*, 512, 2111, doi: [10.1093/mnras/stac319](https://doi.org/10.1093/mnras/stac319)
- Hu, Y., Xu, S., Stone, J. M., & Lazarian, A. 2022b, *ApJ*, 941, 133, doi: [10.3847/1538-4357/ac9ebc](https://doi.org/10.3847/1538-4357/ac9ebc)
- Hu, Y., Yuen, K. H., & Lazarian, A. 2019, *ApJ*, 886, 17, doi: [10.3847/1538-4357/ab4b5e](https://doi.org/10.3847/1538-4357/ab4b5e)
- Jokipii, J. R. 1966, *ApJ*, 146, 480, doi: [10.1086/148912](https://doi.org/10.1086/148912)
- Kandel, D., Lazarian, A., & Pogosyan, D. 2016, *Monthly Notices of the Royal Astronomical Society*, 461, 1227, doi: [10.1093/mnras/stw1296](https://doi.org/10.1093/mnras/stw1296)
- Kovetz, E. D., & Kamionkowski, M. 2015, *Phys. Rev. D*, 91, 081303, doi: [10.1103/PhysRevD.91.081303](https://doi.org/10.1103/PhysRevD.91.081303)
- Kowal, G., Lazarian, A., & Beresnyak, A. 2007, *The Astrophysical Journal*, 658, 423, doi: [10.1086/511515](https://doi.org/10.1086/511515)
- Krumholz, M. R., & McKee, C. F. 2005, *ApJ*, 630, 250, doi: [10.1086/431734](https://doi.org/10.1086/431734)

- Larochelle, H., Erhan, D., Courville, A., Bergstra, J., & Bengio, Y. 2007, in Proceedings of the 24th international conference on Machine learning, ICML '07 & ILP '07 (ACM), doi: [10.1145/1273496.1273556](https://doi.org/10.1145/1273496.1273556)
- Larson, R. B. 1981, *MNRAS*, 194, 809, doi: [10.1093/mnras/194.4.809](https://doi.org/10.1093/mnras/194.4.809)
- Lazarian, A. 2014, *SSRv*, 181, 1, doi: [10.1007/s11214-013-0031-5](https://doi.org/10.1007/s11214-013-0031-5)
- Lazarian, A., Esquivel, A., & Crutcher, R. 2012, *ApJ*, 757, 154, doi: [10.1088/0004-637X/757/2/154](https://doi.org/10.1088/0004-637X/757/2/154)
- Lazarian, A., & Pogosyan, D. 2000, *The Astrophysical Journal*, 537, 720, doi: [10.1086/309040](https://doi.org/10.1086/309040)
- Lazarian, A., & Vishniac, E. T. 1999, *ApJ*, 517, 700, doi: [10.1086/307233](https://doi.org/10.1086/307233)
- Lazarian, A., & Xu, S. 2023, *The Astrophysical Journal*, 956, 63, doi: [10.3847/1538-4357/acea5c](https://doi.org/10.3847/1538-4357/acea5c)
- Lazarian, A., & Yuen, K. H. 2018, *The Astrophysical Journal*, 853, 96, doi: [10.3847/1538-4357/aaa241](https://doi.org/10.3847/1538-4357/aaa241)
- Lazarian, A., Yuen, K. H., & Pogosyan, D. 2020, Obtaining magnetic field strength using differential measure approach and velocity channel maps. <https://arxiv.org/abs/2002.07996>
- . 2022, *The Astrophysical Journal*, 935, 77, doi: [10.3847/1538-4357/ac6877](https://doi.org/10.3847/1538-4357/ac6877)
- Lazarian, A., Yuen, K. H., & Pogosyan, D. 2024, *ApJ*, 974, 237, doi: [10.3847/1538-4357/ad6d62](https://doi.org/10.3847/1538-4357/ad6d62)
- Lecun, Y., Bottou, L., Bengio, Y., & Haffner, P. 1998, *Proceedings of the IEEE*, 86, 2278, doi: [10.1109/5.726791](https://doi.org/10.1109/5.726791)
- Mac Low, M.-M., & Klessen, R. S. 2004, *Reviews of Modern Physics*, 76, 125, doi: [10.1103/RevModPhys.76.125](https://doi.org/10.1103/RevModPhys.76.125)
- McKee, C. F., & Ostriker, E. C. 2007, *Annual Review of Astronomy and Astrophysics*, 45, 565, doi: <https://doi.org/10.1146/annurev.astro.45.051806.110602>
- Mestel, L. 1966, *Monthly Notices of the Royal Astronomical Society*, 133, 265, doi: [10.1093/mnras/133.2.265](https://doi.org/10.1093/mnras/133.2.265)
- Mestel, L., & Spitzer, L., J. 1956, *MNRAS*, 116, 503, doi: [10.1093/mnras/116.5.503](https://doi.org/10.1093/mnras/116.5.503)
- Mignon-Risse, R., González, M., & Commerçon, B. 2023, *A&A*, 673, A134, doi: [10.1051/0004-6361/202345845](https://doi.org/10.1051/0004-6361/202345845)
- Ostriker, E. C., Stone, J. M., & Gammie, C. F. 2001, *ApJ*, 546, 980, doi: [10.1086/318290](https://doi.org/10.1086/318290)
- Padoan, P., Nordlund, A., & Jones, B. J. T. 1997, *MNRAS*, 288, 145, doi: [10.1093/mnras/288.1.145](https://doi.org/10.1093/mnras/288.1.145)
- Passot, T., & Vázquez-Semadeni, E. 1998, *Phys. Rev. E*, 58, 4501, doi: [10.1103/PhysRevE.58.4501](https://doi.org/10.1103/PhysRevE.58.4501)
- Peek, J. E. G., & Burkhart, B. 2019, *ApJL*, 882, L12, doi: [10.3847/2041-8213/ab3a9e](https://doi.org/10.3847/2041-8213/ab3a9e)
- Planck Collaboration:, Ade, P. A. R., Aghanim, N., et al. 2015, *A&A*, 576, A104, doi: [10.1051/0004-6361/201424082](https://doi.org/10.1051/0004-6361/201424082)
- Pogosyan, L. 2014, *Journal of Physics: Conference Series*, 496, 012025, doi: [10.1088/1742-6596/496/1/012025](https://doi.org/10.1088/1742-6596/496/1/012025)
- Schmaltz, T., Hu, Y., & Lazarian, A. 2024, *Monthly Notices of the Royal Astronomical Society*, 528, 3897, doi: [10.1093/mnras/stae146](https://doi.org/10.1093/mnras/stae146)
- Takahashi, R., Matsubara, T., & Uehara, K. 2020, *IEEE Transactions on Circuits and Systems for Video Technology*, 30, 2917–2931, doi: [10.1109/tcsvt.2019.2935128](https://doi.org/10.1109/tcsvt.2019.2935128)
- Tofflemire, B. M., Burkhart, B., & Lazarian, A. 2011, *The Astrophysical Journal*, 736, 60, doi: [10.1088/0004-637X/736/1/60](https://doi.org/10.1088/0004-637X/736/1/60)
- van Dyk, D. A., & Meng, X.-L. 2001, *Journal of Computational and Graphical Statistics*, 10, 1–50, doi: [10.1198/10618600152418584](https://doi.org/10.1198/10618600152418584)
- Van Rossum, G., & Drake, F. L. 2009, *Python 3 Reference Manual* (Scotts Valley, CA: CreateSpace)
- Vázquez-Semadeni, E. 1994, *ApJ*, 423, 681, doi: [10.1086/173847](https://doi.org/10.1086/173847)
- Vázquez-Semadeni, E., Hu, Y., Xu, S., Guerrero-Gamboa, R., & Lazarian, A. 2024, *MNRAS*, 530, 3431, doi: [10.1093/mnras/stae1085](https://doi.org/10.1093/mnras/stae1085)
- Wurster, J., & Li, Z.-Y. 2018, *Frontiers in Astronomy and Space Sciences*, 5, doi: [10.3389/fspas.2018.00039](https://doi.org/10.3389/fspas.2018.00039)
- Xu, S. 2022, *ApJ*, 934, 136, doi: [10.3847/1538-4357/ac7c68](https://doi.org/10.3847/1538-4357/ac7c68)
- Xu, S., Ji, S., & Lazarian, A. 2019, *ApJ*, 878, 157, doi: [10.3847/1538-4357/ab21be](https://doi.org/10.3847/1538-4357/ab21be)
- Xu, S., & Yan, H. 2013, *ApJ*, 779, 140, doi: [10.1088/0004-637X/779/2/140](https://doi.org/10.1088/0004-637X/779/2/140)
- Xu, S., & Zhang, B. 2017, *ApJ*, 835, 2, doi: [10.3847/1538-4357/835/1/2](https://doi.org/10.3847/1538-4357/835/1/2)
- Yan, H., & Lazarian, A. 2002, *Phys. Rev. Lett.*, 89, 281102, doi: [10.1103/PhysRevLett.89.281102](https://doi.org/10.1103/PhysRevLett.89.281102)
- Yan, H., & Lazarian, A. 2008, *ApJ*, 673, 942, doi: [10.1086/524771](https://doi.org/10.1086/524771)
- Yuen, K. H., Ho, K. W., & Lazarian, A. 2021, *ApJ*, 910, 161, doi: [10.3847/1538-4357/abe4d4](https://doi.org/10.3847/1538-4357/abe4d4)
- Yuen, K. H., & Lazarian, A. 2020, *ApJ*, 898, 65, doi: [10.3847/1538-4357/ab9307](https://doi.org/10.3847/1538-4357/ab9307)
- Zhang, J., Hu, Y., & Lazarian, A. 2024, *arXiv e-prints*, arXiv:2411.07080, doi: [10.48550/arXiv.2411.07080](https://doi.org/10.48550/arXiv.2411.07080)